UNIVERSITY OF BIRMINGHAM
University of Birmingham Research at Birmingham

Acoustic microbubble dynamics with viscous effects

Manmi, Kawa; Wang, Qian

DOI:
10.1016/j.ultsonch.2016.11.032

License:
Creative Commons: Attribution-NonCommercial-NoDerivs (CC BY-NC-ND)

Document Version
Peer reviewed version

Citation for published version (Harvard):
Manmi, K & Wang, Q 2016, 'Acoustic microbubble dynamics with viscous effects', *Ultrasonics Sonochemistry*, vol. 36, pp. 427-436. https://doi.org/10.1016/j.ultsonch.2016.11.032

Link to publication on Research at Birmingham portal

General rights
Unless a licence is specified above, all rights (including copyright and moral rights) in this document are retained by the authors and/or the copyright holders. The express permission of the copyright holder must be obtained for any use of this material other than for purposes permitted by law.

•Users may freely distribute the URL that is used to identify this publication.
•Users may download and/or print one copy of the publication from the University of Birmingham research portal for the purpose of private study or non-commercial research.
•User may use extracts from the document in line with the concept of 'fair dealing' under the Copyright, Designs and Patents Act 1988 (?)
•Users may not further distribute the material nor use it for the purposes of commercial gain.

Where a licence is displayed above, please note the terms and conditions of the licence govern your use of this document.

When citing, please reference the published version.

Take down policy
While the University of Birmingham exercises care and attention in making items available there are rare occasions when an item has been uploaded in error or has been deemed to be commercially or otherwise sensitive.

If you believe that this is the case for this document, please contact UBIRA@lists.bham.ac.uk providing details and we will remove access to the work immediately and investigate.

Download date: 23. Mar. 2025

Accepted Manuscript

Acoustic microbubble dynamics with viscous effects

Kawa Manmi, Qianxi Wang

PII: S1350-4177(16)30419-9
DOI: http://dx.doi.org/10.1016/j.ultsonch.2016.11.032
Reference: ULTSON 3446

To appear in: *Ultrasonics Sonochemistry*

Received Date: 12 March 2016
Revised Date: 9 November 2016
Accepted Date: 25 November 2016

Please cite this article as: K. Manmi, Q. Wang, Acoustic microbubble dynamics with viscous effects, *Ultrasonics Sonochemistry* (2016), doi: http://dx.doi.org/10.1016/j.ultsonch.2016.11.032

This is a PDF file of an unedited manuscript that has been accepted for publication. As a service to our customers we are providing this early version of the manuscript. The manuscript will undergo copyediting, typesetting, and review of the resulting proof before it is published in its final form. Please note that during the production process errors may be discovered which could affect the content, and all legal disclaimers that apply to the journal pertain.

ACCEPTED MANUSCRIPT

Acoustic microbubble dynamics with viscous effects

Kawa Manmi [1, 2], Qianxi Wang [2, 3*]

[1]Department of Mathematics - College of Science, Salahaddin University \Erbil, Kurdistan Region, Iraq

[2]School of Mathematics, University of Birmingham, B15 2TT, United Kingdom

3 School of Naval Architecture, Dalian University of Technology, Dalian, 116085, China.

Microbubble dynamics subject to ultrasound are associated with important applications in biomedical ultrasonics, sonochemistry and cavitation cleaning. The viscous effects in this phenomenon is essential since the Reynolds number *R*e associated is about *O*(10). The flow field is characterized as being an irrotational flow in the bulk volume but with a thin vorticity layer at the bubble surface. This paper investigates the phenomenon using the boundary integral method based on the viscous potential flow theory. The viscous effects are incorporated into the model through including the normal viscous stress of the irrotational flow in the dynamic boundary condition at the bubble surface. The viscous correction pressure of Joseph & Wang (J. Fluid Mech., 505, 365-377, 2004) is implemented to resolve the discrepancy between the non-zero shear stress of the irrotational flow at a free surface and the physical boundary condition of zero shear stress. The model agrees well with the Rayleigh–Plesset equation for a spherical bubble oscillating in a viscous liquid for several cycles of oscillation for *R*e = 10. It correlates pretty closely with both the experimental data and the axisymmetric simulation based on the Navier-Stokes equation for transient bubble dynamics near a rigid boundary. We further analyze microbubble dynamics near a rigid boundary subject to ultrasound travelling perpendicular and parallel to the boundary, respectively, in parameter regions of clinical relevance. The viscous effects to acoustic microbubble dynamics are analyzed in terms of the jet velocity, bubble volume, centroid movement, Kelvin impulse and bubble energy.

Key words: Microbubble dynamics; Ultrasound; Bubble jetting; Viscous potential flow theory; Viscous pressure correction; Boundary integral method.

* Corresponding author: q.x.wang@bham.ac.uk

ACCEPTED MANUSCRIPT

1. Introduction

Microbubble dynamics subject to ultrasound are associated with important applications. The medical applications include extracorporeal shock wave lithotripsy [2-8], tissue ablating (histotripsy) [7-11], and oncology and cardiology [12]. In those applications, cavitation microbubbles absorb and concentrate significant amounts of energy from ultrasound, leading to violent collapsing, shock waves and bubble jetting [13]. These mechanisms are also associated with sonochemistry [14-16] and ultrasound cavitation cleaning - one of the most effective cleaning processes for electrical and medical micro-devices [17-18].

The boundary integral method (BIM) is grid free in the flow domain and widely used in simulating bubble dynamics [19-21]. In the BIM the dimension of the problem reduces by one and it thus costs less CPU time as compared to the domain approaches. Acoustic bubble dynamics were simulated using an axisymmetric BIM model for a bubble in an infinite liquid [22-24] and near a boundary subject to ultrasound propagating in the direction perpendicular to the boundary [11, 25-28]. Wang & Manmi [13] studied three dimensional (3D) bubble dynamics near a wall subject to ultrasound propagating parallel to the wall. The above works were based on the inviscid potential flow theory, but the viscous effects may not be negligible for micron size bubbles [29-31].

Transient bubble dynamics including viscous effects were simulated based on the Navier-Stokes equations using the finite volume method (FVM) or finite element method (FEM) [30, 32-36] for axisymmetric cases. It is a multi-scaled problem with the thickness of the viscous boundary layer at the bubble surface is small compared with the bubble radius, and both of them change order of magnitude with time. Simulations of bubble dynamics using FEM or FVM are computationally demanding. As such, simulations based on the domain approaches are usually carried out for only axisymmetric configurations and/or for one cycle of oscillation

Viscous fluid dynamics can be described approximately by potential flows when the vorticity is small or is confined to a narrow layer near the boundary [1, 37]. It is particularly useful for a gas–liquid two-phase flow with an interface. A key issue in the theory is that the shear stress should approximately vanish at a gas-liquid interface, but it does not in the irrotational approximation. An auxiliary function, the viscous pressure correction to the

ACCEPTED MANUSCRIPT

potential pressure, has been introduced to address this discrepancy by Joseph et al. [1, 37]. They argued that the power done by the shear stress due to the irrotational flow should be equal to the power done by the viscous correction pressure to conserve the energy of the system. Accurate physical descriptions of the viscous flows were provided by the viscous potential theory with the viscous pressure correction, including the motion of bubbles and drops [1, 37], capillary instability of a liquid cylinder [38, 39], the decay of free surface waves [37, 39], and the Kelvin-Hemholtz instability [40].

This theory was applied for transient bubble dynamics based on the BIM by Lind & Phillips [30, 41, 42] for transient bubbles near a boundary in an axisymmetric configuration, and by Klaseboer et al. [43] and Zhang & Ni [44] for a bubble rising and deforming in a viscous liquid.

We will model 3D microbubble dynamics in a viscous liquid subject to ultrasound using the viscous potential theory of Joseph et al. [1, 37] based on the following considerations. Firstly, the Reynolds number *R*e for the liquid flow associate with acoustic microbubble dynamics appears large. Re can be estimated as $Re = \rho R_0^2 \omega_M / \mu$, where R_0 is the equilibrium radius of a bubble, ρ and μ are the density and viscosity of the liquid and ω_M is the larger of the natural frequency of the bubble and the ultrasound frequency. The natural frequency of a bubble is $\omega_b = \frac{1}{R_0}\sqrt{\frac{3p_0}{\rho} + \frac{4\gamma}{\rho R_0}}$, where p_0 is the ambient pressure and γ is surface tension. It can be estimated that *R*e ≥ 42 as $R_0 \geq 2$ μm, using the following parameters for water: p_0 = 100 kPa, ρ = 1000 kg m^{-3}, $\mu = 10^{-3}$ Pa s and γ = 0.07 N m^{-1}. Nonspherical microbubble dynamics are thus usually associated with an irrotational flow in the bulk volume but a thin vorticity layer at the bubble surface [45]. Secondly, a microbubble is approximately spherical during most of lifetime due to surface tension [15]. In the case of spherical bubbles, viscosity only enters the analysis through the normal stress on the surface of the bubble but plays no role in the fluid body, apart from viscous dissipation. Physically this is realized in the extra work required to expand the bubble against the additional normal viscous force at the bubble surface [46, 47]. Thirdly, a bubble subject to ultrasound may become nonspherical during a very short period at the end of collapse [13, 23, 24], when the

ACCEPTED MANUSCRIPT

inertial effects are dominant and the viscous effects are not significant.

The remainder of the paper is organized as follows. The physical and mathematical model is described in section 2 based on the BIM and the viscous potential flow theory. In section 3, our numerical model is validated by comparing with the Rayleigh–Plesset equation for spherical bubble oscillating in a unbounded viscous fluid, the experiment [48] and the VOF [49] for the dynamics of a transient bubble near a rigid boundary. In sections 4 and 5, we analyze bubble dynamics near a rigid boundary subject to ultrasound travelling perpendicular and parallel to the boundary, respectively.

2. Physical and mathematical model

Consider the dynamics of a microbubble near an infinite rigid plane wall subject to ultrasound, as shown in figure 1. A Cartesian coordinate system *o-xyz* is set with the origin at the centre of the initial spherical bubble, the *z*-axis perpendicular to the wall (see figure 1a). The acoustic pressure p_∞ parallel to the wall is given as,

$$p_\infty(x,t) = p_0 + p_a \sin(kx - \omega t), \tag{1a}$$

where p_0 is the hydrostatic pressure, x is the coordinate along the propagation direction of the wave, t is time, and p_a, k and ω are the pressure amplitude, wavenumber and angular frequency of the acoustic wave, respectively.

When the wave propagates perpendicular to a rigid boundary, a standing wave is generated if all of the acoustic energy is reflected from the boundary, as assumed here for convenience. A standing wave oriented perpendicular to the boundary (along the *z*-axis) can be described as,

$$p_\infty(z,t) = 1 - p_a \cos\left(k\left(z+s\right)\right)\sin(\omega t), \tag{1b}$$

where s is the distance from the bubble centre at inception to the wall (see figure 1b) .

We assume the system undergoes an adiabatic process, the internal bubble pressure p_B thus can be expressed as:

$$p_B = p_v + p_{g0}\left(\frac{V_0}{V}\right)^{\lambda}, \tag{2}$$

where p_{g0} is the initial gas pressure of the bubble, p_v vapour pressure, V_0 the initial bubble volume and λ the ratio of specific heats of the gas.

ACCEPTED MANUSCRIPT

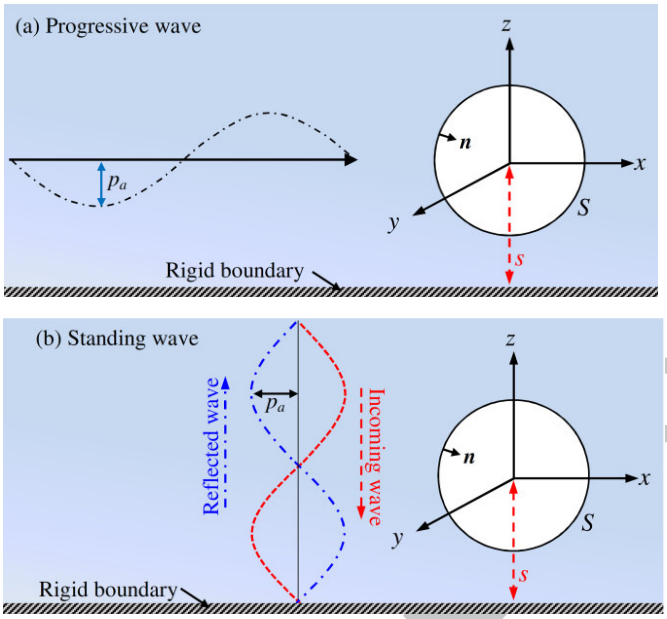

Figure 1. The configuration and coordinate system for a microbubble near a rigid wall subject to ultrasound propagating (a) parallel to the wall or (b) perpendicular on the wall.

We assume that the fluid surrounding the bubble is incompressible and the flow is irrotational. The fluid velocity $\boldsymbol{v}$ thus has a potential φ, $\boldsymbol{v} = \nabla\varphi$, which satisfies Laplace's equation, $\nabla^2\varphi = 0$. Using Green's second identity the potential φ may be represented as a surface integral over the bubble surface S as follows:

$$c(\boldsymbol{r})\varphi(\boldsymbol{r}) = \int_S \left(\frac{\partial\varphi(\boldsymbol{q})}{\partial n} G(\boldsymbol{r},\boldsymbol{q}) - \varphi(\boldsymbol{q}) \frac{\partial G(\boldsymbol{r},\boldsymbol{q})}{\partial n} \right) dS(\boldsymbol{q}), \tag{3}$$

where $\boldsymbol{r}$ is the field point, $\boldsymbol{q}$ the source point, $c(\boldsymbol{r})$ the solid angle and $\boldsymbol{n}$ the unit outward normal at the bubble surface S directed from liquid to gas. To satisfy the impermeable boundary condition on the wall, the Green function is given as follows,

$$G(\boldsymbol{r},\boldsymbol{q}) = \frac{1}{|\boldsymbol{r}-\boldsymbol{q}|} + \frac{1}{|\boldsymbol{r}-\boldsymbol{q}'|}, \tag{4}$$

where $\boldsymbol{q}'$ is the image of $\boldsymbol{q}$ reflected to the wall.

In the viscous potential flow theory (VPF), the normal stress balance at the bubble surface, considering the surface tension and normal viscous stress τ_n, is given as follows:

$$p_L + 2\gamma\kappa - \tau_n = p_B, \quad \tau_n = 2\mu \frac{\partial^2\varphi}{\partial^2 n}, \tag{5}$$

ACCEPTED MANUSCRIPT

where μ is viscosity of the liquid, p_L the liquid pressure at the bubble surface, γ surface tension and κ the local mean curvature of the bubble surface.

The tangential stress at the bubble surface should be zero as a result of the relatively low viscosity of the gas inside the bubble. However, the shear stress due to the irrotational flow is non-zero. Joseph & Wang [1, 34] introduced a viscous pressure correction $p_{\rm vc}$ to resolve the above discrepancy. To satisfy energy conservation for the liquid flow, the viscous pressure correction is set to perform the equal power as the shear stress at the free surface, which leads to the following relation at the bubble surface,

$$\int_S u_n(-p_{\rm vc})\,dS = \int_S \boldsymbol{u}_\tau \cdot \boldsymbol{\tau}_s\,dS\,, \tag{6}$$

where $\boldsymbol{\tau}_s$ is the shear stress at the bubble surface.

This model is called the viscous correction of VPF (VCVPF) [1].The computation results in this paper are based on VCVPF unless stated otherwise. With the pressure correction $p_{\rm vc}$ introduced, the normal stress balance at the bubble surface becomes,

$$p_L + p_{\rm vc} + 2\gamma\kappa - 2\mu\frac{\partial^2\varphi}{\partial n^2} = p_B\,. \tag{7}$$

We assume that the viscous correction pressure $p_{\rm vc}$ is proportional to the normal stress τ_n induced by the irrotational velocity $p_{\rm vc} = -C\tau_n$, where the constant C to be determined by (6). Substituting this into (7) yields

$$p_L + 2\gamma\kappa - 2\mu(1+C)\frac{\partial^2\phi}{\partial n^2} = p_B\,. \tag{8}$$

As shown in (8), the hypothesis $p_{\rm vc} = -C\tau_n$ is equivalent to the assumption that the normal strain rate at the interface is changed by a factor of $1+C$ due to the weak viscous effects. The hypothesis $p_{\rm vc} = -C\tau_n$ with C determined by (6) satisfies energy conservation for the liquid flow globally.

A rational model for the viscous correction is unavailable at the moment. Joseph & Wang [1] assumed that the viscous pressure correction can be expressed by the spherical or ellipsoidal harmonic series, etc. It can be verified that both approaches provide exactly the same results for all the cases discussed in [1], including a rising spherical gas bubble, a spherical liquid drop moving in another liquid and the decay of free surface waves with surface tension, etc.

Our computational results in section 3 based on the viscous pressure correction provided by (8) show good agreement with the experiments and the computations using the Navier-Stokes equation.

ACCEPTED MANUSCRIPT

$\partial^2\varphi/\partial n^2$ needed in (8) can be calculated as follows:

$$\frac{\partial^2 \varphi}{\partial n^2} = \mathbf{n}\cdot\nabla\varphi_n = \mathbf{n}\cdot\frac{\partial}{\partial n}\nabla\varphi = n_x\frac{\partial \varphi_x}{\partial n} + n_y\frac{\partial \varphi_y}{\partial n} + n_z\frac{\partial \varphi_z}{\partial n}, \tag{9}$$

where $\mathbf{n} = (n_x, n_y, n_z)$. φ_x, φ_y, and φ_z satisfy Laplace's equation since φ satisfies Laplace's equation. They thus satisfy the boundary integration equation (3). As a result, we can replace φ in (3) by φ_x, φ_y, and φ_z to formulate the boundary integral equations to find the terms $\partial\varphi_x/\partial n$, $\partial\varphi_y/\partial n$ and $\partial\varphi_z/\partial n$ respectively. Subsequently, $\partial^2\varphi/\partial n^2$ is calculated from (9).

It is inconvenient to calculate $\boldsymbol{\tau}_s$ directly to obtain p_{vc} or C using (6) or (8). This is achieved indirectly by introducing the rate of energy dissipation D [44].

$$D = \int_S \boldsymbol{u}\cdot\boldsymbol{\sigma}\cdot\mathbf{n}ds = \int_S u_n\,\tau_n\,dS + \int_S \boldsymbol{u}_\tau\cdot\boldsymbol{\tau}_s\,dS, \tag{10}$$

where $\boldsymbol{\sigma}$ is stress tensor. Substituting (6) and $p_{\mathrm{vc}} = -C\,\tau_n$ in (10) yields

$$D = (1+C)\int_S u_n\,\tau_n\,dS = 2\mu(1+C)\int_S \frac{\partial\varphi}{\partial n}\frac{\partial^2\varphi}{\partial n^2}dS. \tag{11}$$

On the other hand, the dissipation rate D can be written in the surface integral on the boundary for the irrotational flow [50],

$$D = 2\mu\int_S\left(\varphi_x\frac{\partial\varphi_x}{\partial n} + \varphi_y\frac{\partial\varphi_y}{\partial n} + \varphi_z\frac{\partial\varphi_z}{\partial n}\right)dS. \tag{12}$$

Using (11) and (12) yields

$$C = \frac{\displaystyle\int_S \nabla\varphi\cdot\frac{\partial\nabla\varphi}{\partial n}dS}{\displaystyle\int_S \frac{\partial\varphi}{\partial n}\frac{\partial^2\varphi}{\partial n^2}dS} - 1. \tag{13}$$

The surface integrals in (13) are calculated by using the linear interpolation of φ_x, φ_y, φ_z, $\partial\varphi_x/\partial n$, $\partial\varphi_y/\partial n$, $\partial\varphi_z/\partial n$ and $\partial^2\varphi/\partial n^2$ on each triangular element at the bubble surface S.

We choose the reference length R_0 (initial radius of the bubble) and the reference pressure $\Delta p = p_0 - p_v$. The dimensionless kinematic and dynamic boundary conditions at the bubble surface are as follows:

$$\frac{D\mathbf{r}_*}{Dt_*} = \nabla\varphi_*, \tag{14a}$$

$$\frac{D\varphi_*}{Dt_*} = 1 + \frac{1}{2}\left|\nabla\varphi_*\right|^2 - \varepsilon\left(\frac{V_{*0}}{V_*}\right)^{\lambda} + 2\frac{\kappa}{We} - \frac{2(1+C)}{\mathrm{Re}}\frac{\partial^2\varphi_*}{\partial n^2} + p_{a^*}\sin(k_*x_* - \omega_*t_*), \tag{14b}$$

where the dimensionless variables are denoted with the subscript '*', $\varepsilon = p_{g0}/\Delta p$ is the dimensionless initial pressure of the bubble gas, and the Reynolds number Re and weber

ACCEPTED MANUSCRIPT

number *We* are defined as $Re = R_0\sqrt{\Delta p\ \rho}\ /\ \mu$, $We = \Delta p\, R_0 / \gamma$, where ρ is density of the liquid.

Following the convention the standoff distance is nondimensionalized with respect to the maximum equivalent bubble radius $R_{\max}$,

$$h = \frac{s}{R_{\max}}. \tag{15}$$

The numerical model is based on the BIM. At each time step, we have a known bubble surface and potential distribution φ at the bubble surface. With this information we can calculate the tangential velocity at the bubble surface. The normal velocity at the bubble surface is obtained after solving the boundary integral equation (3), C and $\partial^2\varphi/\partial n^2$ are calculated from (9) and (13). The bubble shape and the potential distribution on it can be further updated by performing the Lagrangian time integration to (14a, b), respectively, using the fourth-order Runge-Kutta scheme (RK4). The details on the numerical model using the BIM for the problem can be found in [13, 51, 52].

The bubble surface and potential distribution were interpolated using a polynomial scheme coupled with the moving least square method for calculating the surface curvature and tangential velocity on the surface [53-55].

A local Cartesian coordinate system for the node say $\boldsymbol{x}_i$, *O-XYZ*, is introduced, with its origin *O* at the point $\boldsymbol{x}_i$, and its *Z*-axis along the normal direction $\boldsymbol{n}_i$. A second order polynomial is implemented for the bubble surface as follows,

$$Z = F(X,Y) = a_1 + a_2X + a_3Y + a_4XY + a_5X^2 + a_6Y^2, \tag{16}$$

The coefficients of the quadratic function are determined by implementing the least-squares fitting with the nearest neighbouring nodes from the node $\boldsymbol{x}_i$. The local mean curvature κ at the node $\boldsymbol{x}_i$ will be calculated from (16) as follows:

$$\kappa(\boldsymbol{x}_i) = -\frac{a_5 + a_6 + a_6a_2^2 + a_5a_3^2 - a_2\,a_3\,a_4}{(1+a_2^2+a_3^2)^{3/2}}. \tag{17}$$

By the same scheme the potential distribution is interpolated as follows:

$$\varphi(X,Y) = b_1 + b_2X + b_3Y + b_4XY + b_5X^2 + b_6Y^2. \tag{18}$$

The tangential velocity $\boldsymbol{v}_\tau$ at node $\boldsymbol{x}_i$ is obtained as

$$\boldsymbol{v}_\tau = b_2\nabla X(x,y,z) + b_3\nabla Y(x,y,z). \tag{19}$$

A high quality surface mesh of the bubble surface is maintained by implementing a hybrid of the Lagrangian method and elastic mesh technique [13]. When the free surface is

ACCEPTED MANUSCRIPT

updated, instead of following the material velocity, the mesh nodes can be convected with the normal velocity plus an prescribed artificial tangential velocity, $\boldsymbol{v}_{\tau}^{pre}$, the sum of which is termed as the prescribed velocity, $\boldsymbol{v}^{pre}$,

$$\boldsymbol{v}^{pre} = \boldsymbol{v}_{\mathrm{n}} + \boldsymbol{v}_{\tau}^{pre}. \tag{20}$$

A suitable artificial tangential velocity distribution improves the mesh quality. Eqs. (14a, b) are then integrated using the prescribed velocity as follows:

$$\frac{\delta \boldsymbol{r}}{\delta t} = \boldsymbol{v}^{pre}, \tag{21a}$$

$$\frac{\delta \varphi}{\delta t} = \frac{\partial \varphi}{\partial t} + \boldsymbol{v}^{pre} \cdot \nabla \varphi = \left(\boldsymbol{v}^{pre} - \boldsymbol{v} \right) \cdot \nabla \varphi + \frac{D\varphi}{Dt}. \tag{21b}$$

Wang C. et al. [56, 57] developed an elastic mesh technique (EMT) to determine the prescribed velocity for improving the mesh quality for the simulation of bubble dynamics. The optimum prescribed velocity $\boldsymbol{v}_i^{pre} = \boldsymbol{v}_i^{emt}$ is obtained by minimizing the elastic energy E_{mesh} in the EMT. In the EMT, the mesh sizes at the bubble surface tend to be uniform but a non-uniform mesh is more suitable for a bubble surface with varying curvature. We therefore implement a hybrid of the Lagrangian and EMT approaches as follows,

$$\boldsymbol{v}_i^{\mathrm{hybird}} = W \boldsymbol{v}_i + (1 - W) \boldsymbol{v}_i^{emt}, \; W \in [0, 1], \tag{22}$$

where W was chosen as 0.7 in this paper.

ACCEPTED MANUSCRIPT

3. Validations of the numerical model

3.1 Comparison with the Rayleigh–Plesset equation

We compare firstly with the Rayleigh–Plesset equation (RPE) for a spherical bubble oscillating freely in an infinite viscous fluid, in response to an initial over pressure. The dimensionless RPE is given as follows for the bubble radius $R_*(t_*)$ [55-57]:

$$R_*\ddot{R}_* + \frac{3}{2}\dot{R}_*^2 = p_{g0*}\left(\frac{R_{0*}}{R_*}\right)^{3\lambda} - 1 - \frac{2We}{R_*} - \frac{4}{Re}\frac{\dot{R}_*}{R_*}. \quad \textbf{(3.1)}$$

The parameters for the case are chosen as $R_0 = 4.5$ μm, $\varepsilon = 100$, $p_0 = 101.3$ kPa, $\rho = 999$ kg m^{-3}, $\lambda = 1.67$ and $\gamma = 0.073$ N m^{-1}. A relatively small value of $Re = 10$ is chosen to see the viscous effects evidently in terms of radial oscillation. Figure 2 compares the time histories of the bubble radius as determined from the BIM and RPE. The BIM agrees excellently with the RPE for the first six cycles of oscillation. The amplitude and period of oscillation decrease obviously due to the viscous damping effects, where the maximum radius decreases with cycles yet the minimum radius increases with cycles. The accumulation viscous effects are significant for microbubbles in multiple cycles of oscillation.

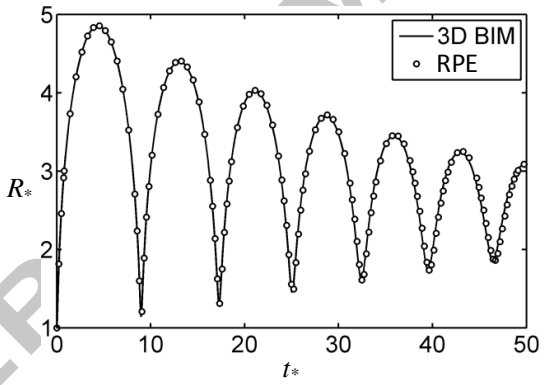

Figure 2. Comparison of the time histories of the radius of a bubble oscillating in an infinite viscous fluid as determined from the 3D BIM and Rayleigh–Plesset equation (RPE). The parameters used for the case are $R_0 = 4.5$ μm, $\varepsilon = 100$, $p_0 = 101.3$ kPa, $\rho = 999$ kg m^{-3}, $\lambda = 1.67$, $\gamma = 0.073$ N m^{-1} and $Re = 10$.

3.2 Comparisons with experiments and VOF

Ohl et al. [48] carried out carefully controlled experiments for a laser-induced gas bubble in water near a rigid boundary for $h = 1$ and $R_{max} = 1$ mm, capturing the detailed behaviour with a high-speed camera. Minsier et al. [33] simulated this case using the

ACCEPTED MANUSCRIPT

axisymmetric VOF model based on the Navier-Stokes equations, with the initial conditions of R_0 = 0.2 mm and p_{g0} = 42 bar, T_{amb} = 300 K and T_{c0} = 2298 K, where T_{amb} is the ambient temperature in the liquid and T_{c0} is the temperature at the centre of the bubble. We will compare the BIM with the experiments and the VOF model.

In the BIM, the same initial pressure as Minsier et al. [33] is chosen however a slightly bigger initial radius R_0 = 0.224 mm is used so that the maximum bubble radius reaches 1 mm. This difference is due to the fact that some thermodynamic energy is set in the VOF simulation by Minsier et al. [33]. The rest of parameters are λ = 1.4, p_0 = 101.3 kpa, ρ = 998 kg m^{-1} and μ_{water} = 0.001 $kgm^{-1}s^{-1}$.

The bubble images were accurately reproduced by both the two numerical models at representative times during the expansion phase, collapse phase and jet formation as shown in figures 3a, 3b and 3c respectively. The oscillation periods of the two computational models are close to each other but are both slightly larger than the experimental data. As such, the corresponding bubble shapes are provided at slightly different times in the two computational models and the experiment. The rigid boundary for h = 1.0 is located at the lower border of each frame. The bubble first expands in a spherical shape except the lower part of the bubble surface is flattened by the boundary at the end of expansion (figure 3a). It then collapses, with the lower part kept attached to the boundary and the rest of the bubble surface collapses approximately spherically (figure 3b). Near the end of collapse, a liquid jet forms and develops rapidly at the top of the bubble surface pointing to the boundary (figure 3c).

a. Expansion phase

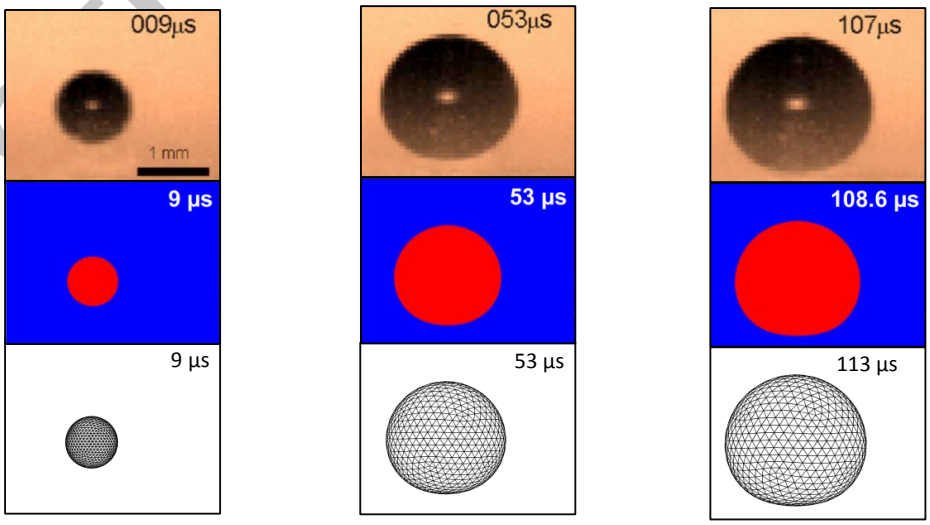

ACCEPTED MANUSCRIPT

b. Collapse phase

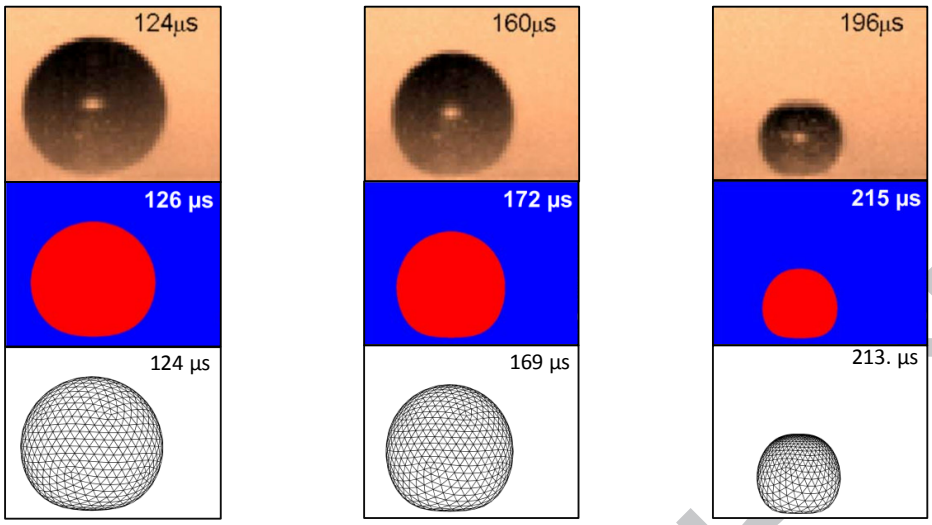

c. Jet formation

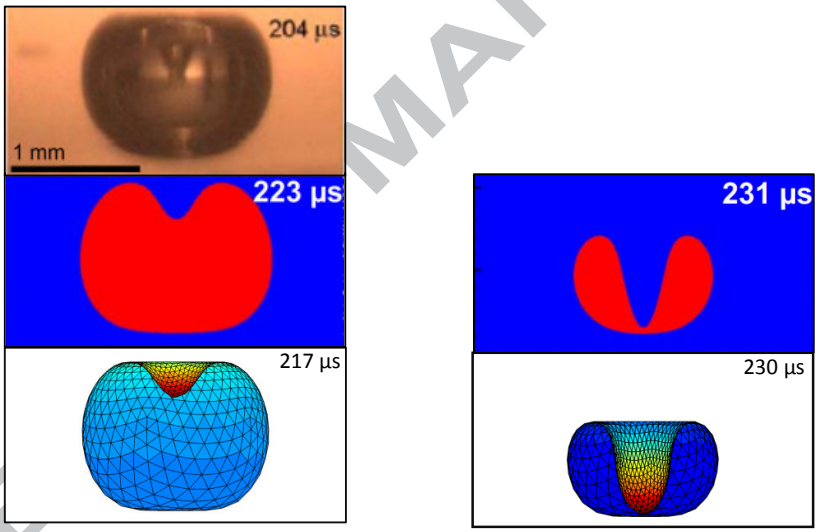

Figure 3. Comparison of the bubble shapes as obtained from the experiments (Ohl et al. [48], in the first row of each phase), VOF (Minsier et al. [33], in the second row) and 3D BIM (in the third-row). The bubble shapes are shown during (a) the expansion phase, (b) collapse phase and (c) jet formation. The rigid boundary is located at the lower borders of frames. The parameters in the 3D BIM are chosen as $R_0 = 0.224$ mm, $p_{g0} = 42$ bar, $h = 1.0$, $\mu_{water} = 0.001$ kg (m s)$^{-1}$, $p_\infty = 101.3$ Kpa, $\rho = 998$ kg m^{-1} and $\lambda = 1.4$.

ACCEPTED MANUSCRIPT

We next compare the 3D BIM and VOF [33] for a bubble collapsing in water with viscosity $\mu_{water} = 0.001$ kg (m s)$^{-1}$ and in an oil with viscosity $\mu_{oil} = 0.05$ kg (m s)$^{-1}$, close to the rigid wall for $h = 0.6$. The corresponding Re numbers for the two cases are $Re = 10000$, 200 respectively. Figures 4a and 4b show the bubble shapes in water and oil, respectively, at representative times at the maximum volume (frame 1 of each row), during the early stage of collapse (frame 2), at the starting of jetting (frame 3) and at the end of collapse (frame 4), respectively. The corresponding bubble shapes of the two models are provided at slightly different times due to the slight different oscillation periods associated. The two models are in very good agreement during the whole collapse phase for both liquids in terms of bubble shapes and jet shapes at corresponding times. The bubble keeps in contact with the boundary and a jet forms and develops quickly at the end of collapse. The jet will impact on the boundary once it penetrates through the bubble. The bubble shape at the end of collapse is smaller in oil and jet is sharper in water. All the above features have been reproduced by the two models.

(a) Numerical results in water

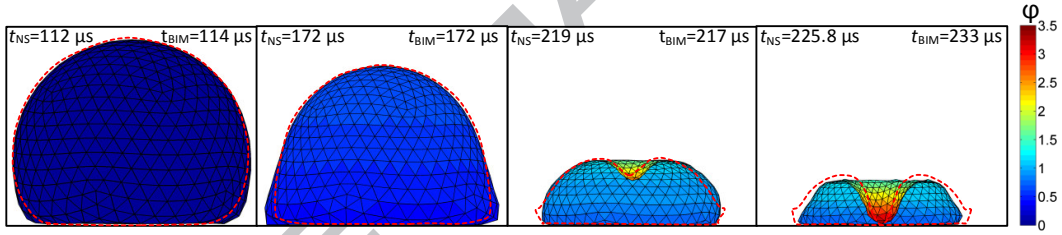

(b) Numerical results in oil

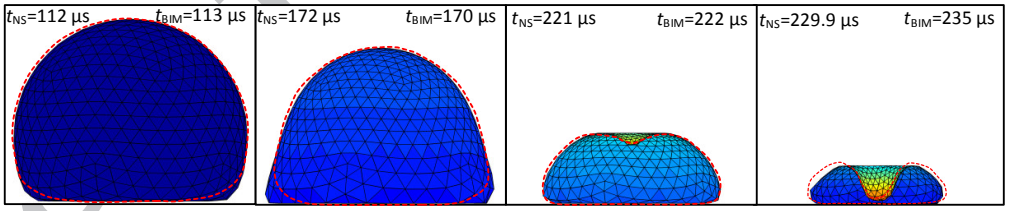

Figure 4. Comparison of the 3D BIM and VOF (Minsier et al. [33], dash line) for a bubble collapsing near a rigid boundary for $h = 0.6$ in (a) water with $\mu_{water} = 0.001$ kg (m s)$^{-1}$ and (b) oil with $\mu_{oil} = 0.05$ kg (m s)$^{-1}$, respectively. The rigid boundary is located at the bottoms of the frames. Other parameters used for the calculation are the same as in figure 3.

Figure 5 shows the comparison of the maximum jet velocities versus the dimensionless standoff distance γ for a bubble in oil near a rigid boundary for the case in figure 4b, obtained using the VOF [33] and 3D BIM . We have consider three BIM models based on the inviscid potential flow theory (IPF), the viscous potential flow theory (VPF), and the viscous

ACCEPTED MANUSCRIPT

correction of VPF (VCVPF), respectively. The results of all the three BIM models agree with the VOF in magnitude and trend in general. The maximum jet velocity reduces due to the normal viscous stress and reduces further due to the viscous pressure correction. The results of VCVPF are closest to the results of the VOF among the three BIM models.

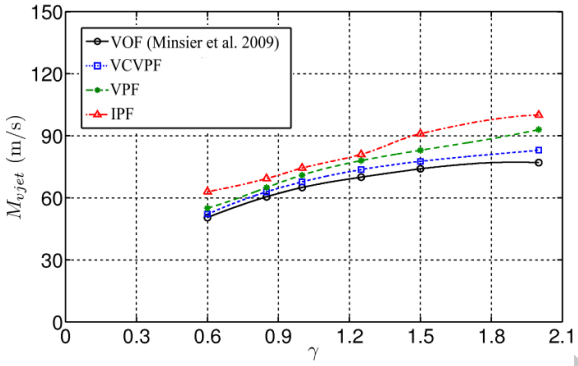

Figure 5. Comparison of the maximum jet velocities M_{vjet} versus the dimensionless stand-off distance γ for a bubble in oil near a rigid boundary for the case in figure 4b, obtained using the VOF [33], 3D BIM models based on the inviscid potential flow theory (IPF), the viscous potential flow theory (VPF) and the viscous correction of VPF (VCVPF), respectively.

4. Microbubble dynamics near a wall subject to ultrasound perpendicular to the wall

Consider a bubble with a radius R_0 = 4.5 μm near a wall with the dimensionless standoff distance h = 1, 2, respectively, subject to ultrasound perpendicular to the wall with the amplitude p_{a*} = 1.4 and frequency f = 300 kHz. Other parameters used are: λ = 1.4, γ = 0.055 N m^{-1}, ρ = 1000 kg m^{-3}, p_0 = 100 kPa, μ = 0.0035 kg (m s)$^{-1}$ and c = 1500 m s^{-1}. The parameters are chosen for blood relevant to biomedical applications. The corresponding Reynolds number is Re = 13. Two other values of Re = 50 and ∞ are examined, to investigate the influence of viscous effects.

Figure 6 shows bubble shapes just before jet impact on the opposite bubble surface for the cases. In both cases h = 1, 2 the jet is directed to the rigid boundary. The red dot in the figures represents centre of the initial bubble. Note that the centre of initial bubble surface is outside of the frames in figure 6b. At a lower Reynolds number Re the jet becomes sharper and the bubble migration to the wall is slowed down because of the viscous effects. The changes are obvious from as Re decreases from 50 to 13, but not significantly as Re decreases from ∞ to 50. The oscillation period of the bubble increases with Re and decreases with h.

ACCEPTED MANUSCRIPT

a. h = 2.0

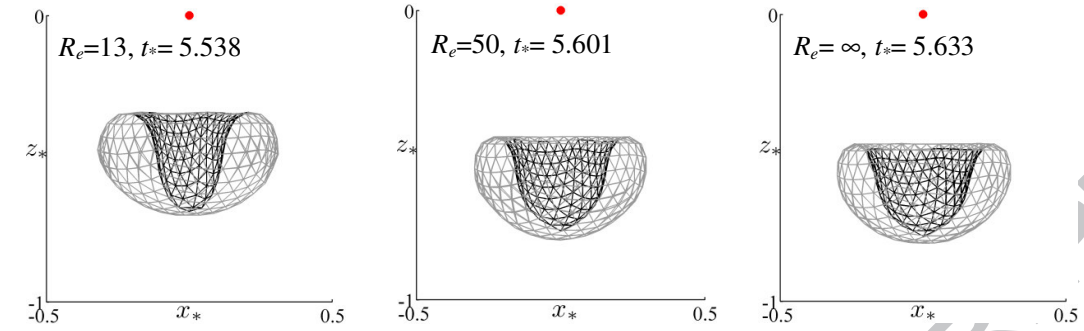

b. h = 1.0

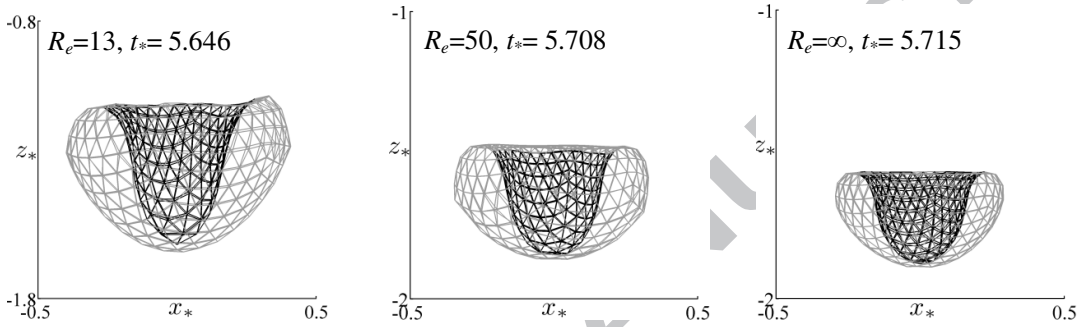

Figure 6. Bubble shapes at jet impact for a bubble near a rigid boundary for the dimensionless standoff distances (a) h = 2 and (b) h = 1, subject to ultrasound perpendicular to the boundary for p_{a*} = 1.4 and f = 300 kHz, and the Reynolds numbers Re = 13, 50 and ∞, respectively. The remaining parameters are R_0 = 4.5 μm, λ = 1.4, γ = 0.055 N m^{-1}, ρ = 1000 kg m^{-3}, p_0 = 100 kPa and c = 1500 m s^{-1}. The red dot in the figures represents centre of the initial bubble.

As shown in Table 1, the maximum equivalent bubble radius R_{max*} and jet velocity V_{jet*} reduce about 6% and 17% respectively, as R_e changes from ∞ to 13 for both h due to the viscous effects. The displacement of the bubble centroid Z_{c*} decreases about 18% and 22% for h = 2 and 1 respectively. The magnitude of the Kelvin impulse and bubble energy at jet impact decrease significantly due to the viscous effects. The changes for all the quantities are relatively large as Re changes from 50 to 13, but much smaller as Re changes from ∞ to 50. This suggests that the viscous effects are small as Re is 50 or larger for the cases considered.

The jet velocity for Re = 13 is about 230 ms^{-1} and 330 m s^{-1} as h = 1, 2 respectively, increasing rapidly with h, whereas the radius of the middle cross-section of the jet are about 16% R_0 and 11% R_0 (figure 6), decreasing with h. For h = 1, the jet tip is about 1.9 μm away from the boundary at jet impact on the opposite bubble surface. It will subsequently penetrate the liquid between the bubble and the boundary and impact on the boundary. This high speed liquid jet has clear potential to damage/penetrate the boundary. However, in the real situation, the jet speed will be attenuated or re-directed by the elastic deformation of the boundary [61, 62].

ACCEPTED MANUSCRIPT

Re	$h = 2$					$h = 1$				
	R_{max*}	V_{jet*}	Z_{c*}	I_{maxk*}	E_{max*}	R_{max*}	V_{jet*}	Z_{c*}	I_{maxk*}	E_{max*}
13	2.07	32.5	-0.70	1.05	61	2.02	23.3	-1.85	2.72	57
50	2.17	38.7	-0.83	1.83	82	2.11	27.6	-2.29	4.32	75
∞	2.20	39.2	-0.85	2.17	91	2.14	28.0	-2.37	4.92	85

Table 1. The maximum equivalent bubble radius R_{max*}, jet velocity V_{jet*}, bubble centroid displacement Z_{c*} along the z-axis, magnitude of the Kelvin impulse I_{maxk*} and bubble energy E_{max*} at jet impact for the cases shown in figure 6.

Ultrasound has emerged as a promising means to affect controlled delivery of therapeutic agents through cell membranes [10, 62-64]. The bubble dynamics generates a rapid flow of liquid around the bubble in the local region at the scale of the bubble size, due to the rapid expansion, collapse, jetting and shock waves emitted at the end of collapse. These phenomena generate oscillating normal and shear stresses on membranes nearby, thus enhancing permeability of lipid bilayers.

5. Microbubble dynamics near a wall subject to ultrasound parallel to the wall

We next consider the cases where ultrasound propagating parallel to the boundary, with the dimensionless standoff distance h = 12, 4 and 1, respectively, and the amplitude of ultrasound p_{a*} = 1.6. The remaining parameters are the same as in figure 6. A high-speed liquid jet develops towards the end of collapse as shown in figure 7, in which the ultrasound propagates from left to right. The oscillation period reduces slightly with the viscous effects.

The acoustic radiation forces on gas bubbles are normally referred to as the Bjerknes forces [65]. The Bjerknes forces have two types: the Bjerknes force is experienced by a single bubble due to pressure gradients in the liquid and the secondary Bjerknes forces are responsible for the bubble-wall and bubble-bubble interactions [66]. The bubble is subject to the Bjerknes force due to the acoustic wave along the wave direction and the second Bjeknes force pointing to the boundary. The jet is along the wave direction for h = 12 (figure 7a), as the effect of the boundary is negligible in this case. The jet is along the bisector of the two Bjerknes forces for h = 4 (figure 7b) when the two forces are comparable, and is pointing to the boundary for h = 1 (figure 7c) as the second Bjerknes force is predominant in this case. More cases calculated but not presented here show that the jet is pointing to the boundary as $h \lesssim 1.5$ and is along the acoustic wave direction as $h \gtrsim 10$. These trends are similar to the cases for $Re = \infty$ [13]. The radius of the middle cross-section of the jet for Re = 13 is 5%, 7% and 20% of the initial radius R_0 for h = 12, 4 and 1, respectively.

ACCEPTED MANUSCRIPT

a. h=12.0

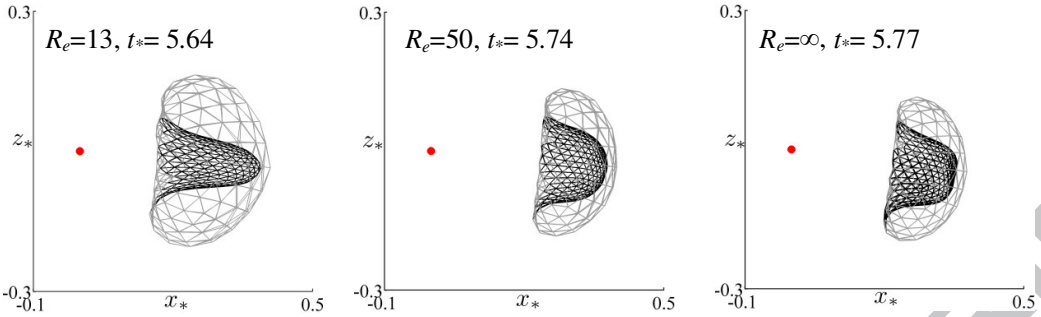

b. h=4.0

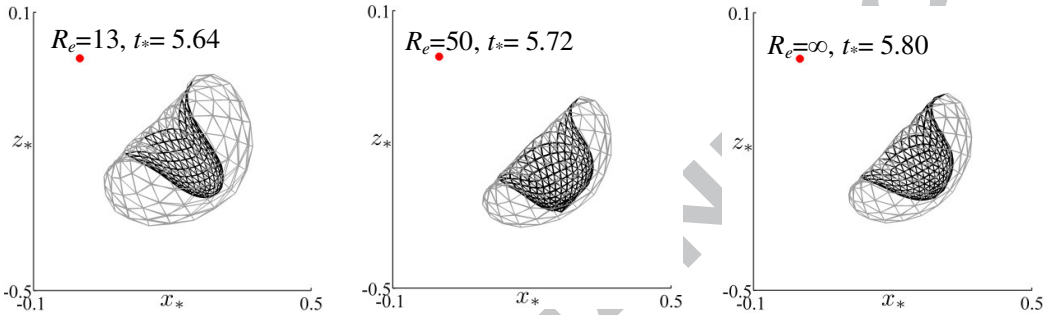

c. h=1.0

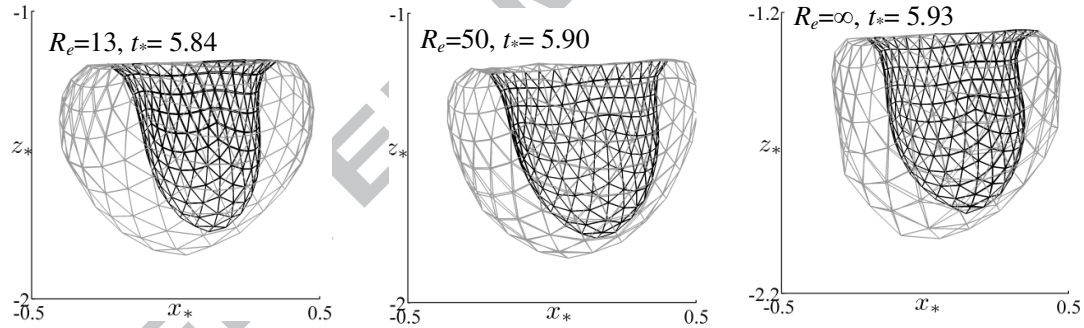

Figure 7. Bubble shapes at jet impact for a bubble near a wall for the dimensionless standoff distances (a) h = 12, (b) h = 4.0 and (c) h = 1.0, subject to ultrasound propagating parallel to the wall for p_{a*} = 1.6 and f = 300 kHz, and the Reynolds numbers Re = 13, 50, and ∞, respectively. The remaining parameters are the same as in figure 6. The direction of ultrasound propagation is from left to right.

After the jet impacts on the opposite bubble surface, the bubble can continue to collapse in a toroidal form, when the liquid flow domain becomes doubly connected. Toroidal bubbles are outside the scope of the present paper. The doubly connected domain can be made singly connected by using a vortex sheet [67, 68] or a branch cut [69]. Wang et al. [70, 71] developed a vortex ring model for the topological transition of a singly connected bubble to a

ACCEPTED MANUSCRIPT

doubly connected toroidal bubble. Zhang et al. [54], Zhang & Liu [72] modelled 3D toroidal bubbles using the vortex ring model.

Figure 8 depicts the time histories of the some global quantities of the bubble for the cases for h = 4 shown in figure 8b. The maximum equivalent bubble radius decreases about 6% as Re is decreased from ∞ to 13 (figure 8a). The maximum jet velocity decreases substantially from 1310 m/s to 930 m/s with the decrease in Re (figure 8b). The centroid movement, the energy and the Kelvin impulse of the bubble increase with Re (figures 8c-f). These trends are associated with the viscous damping effects for a lower Re number.

Similar trends have been observed for h = 12 and 1 as shown in table 2. The maximum equivalent bubble radius R_{max*} reduces about 6% as Re changes from ∞ to 13 for both h due to the viscous effects. The movement of the centroids decreases due to the viscous effects. The maximum Kelvin impulse I_{kmax*} decreases about 26% and 33% for h = 12 and h = 1 respectively with the change in Re, the maximum energy E_{max*} reduces about 10% and 6% respectively. The changes for all the quantities are relatively large as Re changes from 50 to 13, but much smaller as Re changes from ∞ to 50.

The jet velocity for Re = 13 reaches 900 m s^{-1} as h = 4 or larger, deceases rapidly with the standoff distance to about 260 m s^{-1} for h = 1. At the same parameters for a standing wave in the direction perpendicular to the wall, the jet velocity is about 264 m s^{-1} for h =1 and p_{a*} = 1.6. So the jet velocity does not change significantly with the wave direction.

ACCEPTED MANUSCRIPT

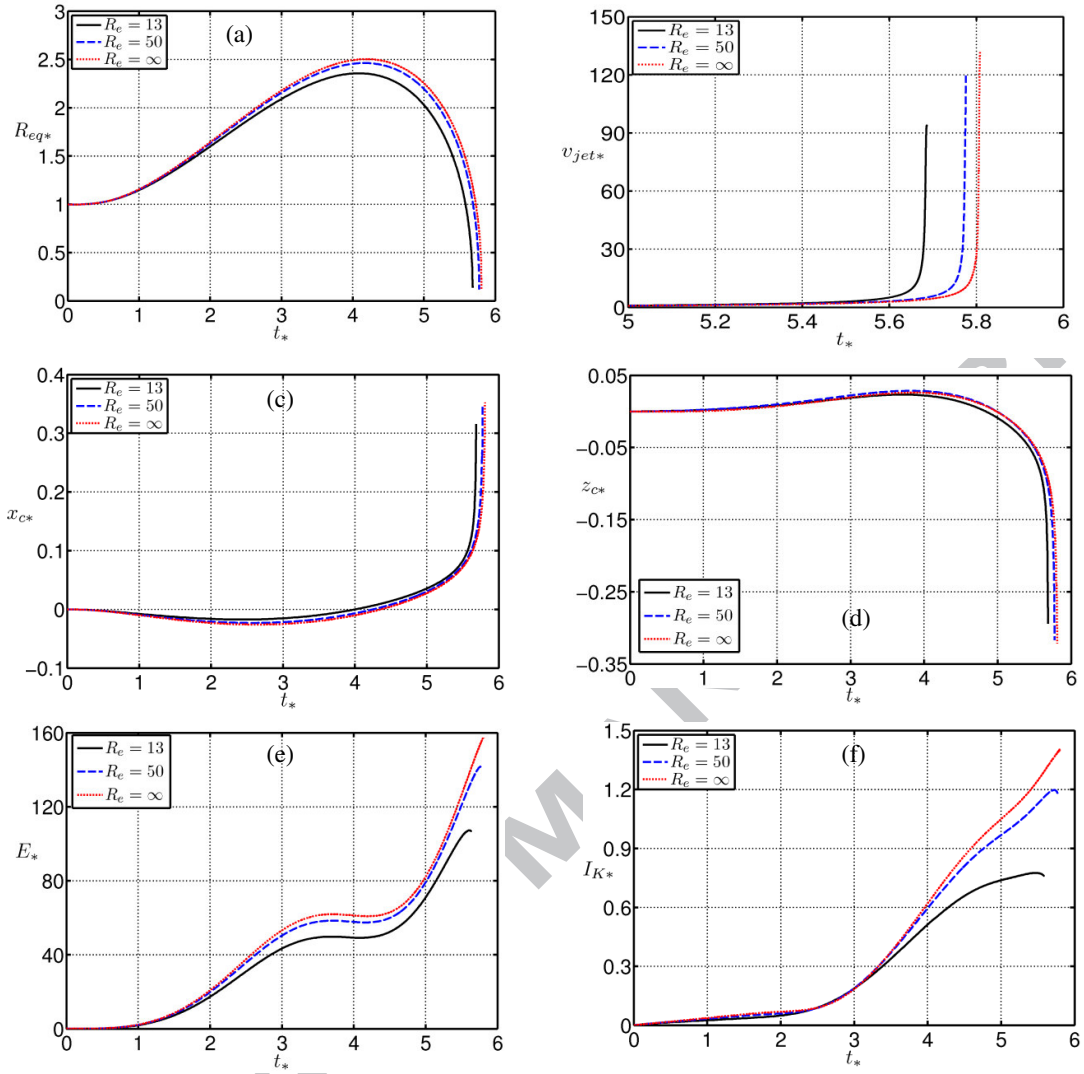

Figure 8. Time histories of (a) the equivalent radius R_{eq*}, (b) jet velocity v_{jet*}, (c) x-component x_{c*} of the centroid, (d) z-component z_{c*} of the centroid, (e) energy E_*, and (f) magnitude of the Kelvin impulse I_{K*} of the bubble for the cases in figure 7b.

R_e	h = 12						h = 1.0					
	R_{max*}	V_{jet*}	X_{c*}	Z_{c*}	I_{kmax*}	E_{max*}	R_{max*}	V_{jet*}	X_{c*}	Z_{c*}	I_{kmax*}	E_{max*}
13	2.39	104	0.37	-0.036	0.71	102	2.25	26.3	0.07	-2.03	4.38	92
50	2.50	138	0.40	-0.041	0.97	147	2.35	28.2	0.10	-2.20	6.51	115
∞	2.54	146	0.43	-0.067	1.09	163	2.38	28.3	0.10	-2.03	7.30	122

Table 2. The maximum equivalent radius R_{max*}, jet velocit V_{jet*}, centroid displacements X_{c*}, Z_{c*}, magnitude of the Kelvin impulse I_{kmax*}, and energy E_{max*} of the bubble at jet impact for the cases in figures 8a, 8c.

ACCEPTED MANUSCRIPT

6. Summary and conclusions

Microbubble dynamics are usually associated with an irrotational flow in the bulk volume but a thin vorticity layer at the bubble surface. This phenomenon has thus been studied using the BIM based on the viscous potential flow theory. The viscous effects are incorporated into the model through including the normal viscous stress due to the irrotational flow and the viscous correction pressure in the dynamic boundary condition at the bubble surface.

The BIM model agrees well with the Rayleigh–Plesset equation for a spherical bubble oscillating in a viscous liquid for several cycles of oscillation at $Re = 10$. It correlates well to the experiments for transient bubble dynamics near a rigid boundary. We have compared the maximum velocity of the bubble jet at $Re = 200$ calculated using the axisymmetric VOF model [33] and the BIMs based on the inviscid potential flow theory (IPF), viscous potential flow theory (VPF) and the viscous correction of VPF (VCVPF), respectively. The results of all the three BIMs correlate with the VOF in general. The jet velocity obtained using the VPF is smaller than the IPF and the jet velocity obtained using the VCVPF is smallest and closest to the VOF.

We have analysed dynamics of a bubble for an equilibrium radius 4.5 μm near a rigid boundary subject to ultrasound for the amplitude 1.4-1.6 p_{atm} and frequency 300 KHz, which are in parameter regions of clinical relevance. The observed features observed may be summarized as follows.

1. The bubble absorbs and concentrates energy from ultrasound, resulting violent collapsing and jetting with a velocity at $O(10^2)$ ms^{-1}. The jet velocity decreases but with a larger cross-section due to the presence of the rigid boundary.
2. The jet is directed to the boundary when the ultrasound is perpendicular to the boundary. When the ultrasound is parallel to the boundary, the jet is directed towards the boundary as the dimensionless standoff distance h of the bubble from the boundary in terms of the maximum bubble radius is as $h \lesssim 1.5$, along the acoustic wave direction as $h \gtrsim 10$ and along the bisector of the two directions around $h \approx 3.75$.
3. The jet direction does not change significantly due to the viscous effects. The oscillation amplitude and period of the bubble decrease with the viscous effects.

ACCEPTED MANUSCRIPT

References

[1] D.D. Joseph, J. Wang, The dissipation approximation and viscous potential flow. Fluid Mech., 505 (2004) 365-377.

[2] M. Delius, R. Denk, C. Berding, H.G. Liebich, M. Jordan, W. Brendel, Biological effects of shock waves: Cavitation by shock waves in piglet liver. Ultrasound in medicine & biology. 16(5) (1990) 467-472.

[3] E. Klaseboer, C.K. Turangan, B.C. Khoo, A.J. Szeri, M.L. Calvisi, G.N. Sankin, P. Zhong, Interaction of lithotripter shockwaves with single inertial cavitation bubbles. J. Fluid Mech. 593 (2007) 33–56.

[4] J.I. Iloreta, N. Fung, A.J. Szeri, Dynamics of bubbles near a rigid surface subjected to a lithotripter shock wave. Part 1. Consequences of interference between incident and reflected waves. J. Fluid Mech. 616 (2008) 43–61.

[5] M.L. Calvisi, J.I. Iloreta, A.J. Szeri, Dynamics of bubbles near a rigid surface subjected to a lithotripter shock wave: II. Reflected shock intensifies non-spherical cavitation collapse. J. Fluid Mech. 616 (2008) 63–97.

[6] A.R. Jamaluddin, G.J. Ball, C.K. Turangan, T.G. Leighton, The collapse of single bubbles and approximation of the far-field acoustic emissions for cavitation induced by shock wave lithotripsy. Journal of Fluid Mechanics, 677 (2011), 305-341.

[7] T.G. Leighton, F. Fedele, A.J. Coleman, C. Mccarthy, S. Ryves, A.M. Hurrella. De Stefano, P.R. White, A passive acoustic device for real-time monitoring the efficacy of shockwave lithotripsy treatment. Ultrasound in Medicine & Biology, 34 (10) (2008) 1651-1665.

[8] T.G. Leighton, C.K. Turangan, A.R. Jamaluddin, G.J. Ball, P.R. White, Prediction of far-field acoustic emissions from cavitation clouds during shock wave lithotripsy for development of a clinical device. Proceedings of the Royal Society A: Mathematical, Physical and Engineering Sciences, 469 (2150) (2013) 20120538.

[9] W.W. Roberts, T.L. Hall, K. Ives, J.S. Wolf JR, J.B. Fowlkes, C.A. Cain, Pulsed cavitational ultrasound: a noninvasive technology for controlled tissue ablation (histotripsy) in the rabbit kidney. The Journal of urology, 175(2) (2006) 734-738.

[10] C. Coussios, R.A. Roy, Applications of acoustics and cavitation to noninvasive therapy and drug delivery. Ann. Rev. Fluid Mech. 40 (2008) 395-420.

[11] G.A. Curtiss, D.M. Leppinen, Q.X. Wang, J.R. Blake, Ultrasonic cavitation near a tissue layer," J. Fluid Mech. 730 (2013) 245-272.

[12] T.A. Leslie, J.E. Kennedy, High-intensity focused ultrasound principles, current uses, and potential for the future. Ultrasound Quart 22 (2006) 263–272.

[13] Q.X. Wang, K. Manmi, Three dimensional microbubble dynamics near a wall subject to high intensity ultrasound. Phys. Fluids (1994-present) 26(3) (2014) 032104.

[14] K.S. Suslick, Sonochemistry. Science 247 (1990) 1439–1445.

[15] T.G. Leighton, Bubble population phenomena in acoustic cavitation. Ultrasonics Sonochemistry, 2 (2) (1995) S123-S136.

[16] P.R. Birkin, T.G. Leighton, Y.E. Watson, The use of acoustoelectrochemistry to investigate rectified diffusion. Ultrasonics Sonochemistry, 11 (3-4) (2004) 217-221.

[17] W.D. Song, M.H. Hong, B. Lukyanchuk, T.C. Chong, Laser-induced cavitation bubbles for cleaning of solid surfaces. J. Appl. Phys. 95 (6) (2004) 2952.

[18] C.D. Ohl, M. Arora, R. Ikink, N. De Jong, M. Versluis, M. Delius D. Lohse, Sonoporation from jetting cavitation bubbles. Biophys. J. 91 (2006a) 4285-4295.

[19] J.R. Blake, B.B. Taib, G. Doherty, Transient cavities near boundaries. Part 1. Rigid Boundary. J. Fluid Mech. 170 (1986) 497.

[20] J.R. Blake, B.B. Taib, G. Doherty, Transient cavities near boundaries. Part 2. Free surface. J. Fluid Mech. 181(1987)197.

ACCEPTED MANUSCRIPT

[21] G.L. Chahine, T.O. Perdue, Simulation of the three-dimensional behaviour of an unsteady large bubble near a structure. in Proc. 3rd Intl Colloq. on Drops and Bubbles, edited by Taylor G. Wang, (American Institute of Physics, New York) (1988).

[22] M.L. Calvisi, O. Lindau, J.R. Blake A.J. Szeri, Shape stability and violent collapse of microbubbles in acoustic traveling waves. Phys. Fluids 19 (2007) 047101.

[23] Q.X. Wang, J.R. Blake, Non-spherical bubble dynamics in a compressible liquid. Part 1. Travelling acoustic wave. J. Fluid Mech. 659 (2010) 191-224.

[24] Q.X. Wang, J.R. Blake, Non-spherical bubble dynamics in a compressible liquid. Part 2. Acoustic standing wave. J. Fluid Mech. 679 (2011) 559-581.

[25] E. Klaseboer, B.C. Khoo, Boundary integral equations as applied to an oscillating bubble near a fluid-fluid interface. Computational Mechanics 33 (2004a) 129–138.

[26] E. Klaseboer, B.C. Khoo An oscillating bubble near an elastic material. Journal of Applied Physics 96 (10) (2004b) 5808–5818.

[27] S.W. Fong, E. Klaseboer, C.K. Turangan, B.C. Khoo, K.C. Hung, Numerical analysis of a gas bubble near biomaterials in an ultrasound field. Ultrasound in Medicine and Biology 32 (6) (2006) 925–942.

[28] S.W. Fong, E. Klaseboer, B.C. Khoo, Interaction of microbubbles with high intensity pulsed ultrasound. J. Acoust. Soc. Am. 123(3) (2008) 1784-1793.

[29] T. Leighton, The Acoustic Bubble. Academic Press, London. 1994 (doi: 10.1017/S0022112094214519).

[30] S. Popinet, S. Zaleski, Bubble collapse near a solid boundary: a numerical study of the influence of viscosity. Journal of Fluid Mechanics, 464 (2002) 137-163.

[31] S.J. Lind, T.N. Phillips, The influence of viscoelasticity on the collapse of cavitation bubbles near a rigid boundary. Theoret. & Comput. Fluid Dyn. 26(1-4) (2012) 245-277.

[32] S.J. Kim, K.H. Lim, C. Kim, Deformation characteristics of spherical bubble collapse in Newtonian fluids near the wall using the finite element method with ALE formulation. Korea-Australia Rheology Journal, 18(2) (2006) 109-118.

[33] V.J. Minsier, De. Wilde, J. Proost, Simulation of the effect of viscosity on jet penetration into a single cavitating bubble. Journal of Applied Physics, 106(8) (2009) 084906.

[34] C. Chen, Y. Gu, J. Tu, X. Guo, D. Zhang, Microbubble oscillating in a microvessel filled with viscous fluid: A finite element modeling study. Ultrasonics 66 (2016) 54-64.

[35] J. Hua, J. Lou, Numerical simulation of bubble rising in viscous liquid. Journal of Computational Physics, 222(2), (2007) 769-795.

[36] M. Gumulya, J.B. Joshi, R.P. Utikar, G.M. Evans, V. Pareek, Bubbles in viscous liquids: Time dependent behaviour and wake characteristics. Chemical Engineering Science, 144 (2016) 298-309.

[37] D.D. Joseph, T. Funada, J. Wang, Potential flows of viscous and viscoelastic fluids. Cambridge University Press (2007).

[38] J. Wang, D.D. Joseph, T. Funada, Viscous contributions to the pressure for potential flow analysis of capillary instability of viscous fluids. Phys Fluids 17(5) (2005): 052105.

[39] J. Wang, D.D. Joseph, Purely irrotational theories of the effect of the viscosity on the decay of free gravity waves. J. Fluid Mech. 559 (2006) 461–472.

[40] J.C. Padrino, D.D. Joseph, H. Kim, Viscous effects on Kelvin–Helmholtz instability in a channel. J. Fluid Mech. 680 (2011) 398- 416.

[41] S.J. Lind, T.N Phillips, T. N. The effect of viscoelasticity on a rising gas bubble. Journal of non-Newtonian fluid mechanics 165(15-16) (2010),852-865.

[42] S.J. Lind, T.N Phillips, The effect of viscoelasticity on the dynamics of gas bubbles near free surfaces. Physics of Fluids 25(2) (2013) 022104-022135.

[43] E. Klaseboer, R. Manica, D.Y.C. Chan, B.C. Khoo, BEM simulations of potential flow with viscous effects as applied to a rising bubble. Engg. Analysis Boundary Elements 35 (2011) 489-494.

ACCEPTED MANUSCRIPT

[44] A.M. Zhang, B.Y. Ni, Three-dimensional boundary integral simulations of motion and deformation of bubbles with viscous effects. Computers & Fluids 92 (2014) 22-33.

[45] T.S. Lundgren, N.N. Mansour, Oscillations of drops in zero gravity with weak viscous effects. Journal of Fluid Mechanics, 194 (1988) 479-510.

[46] F.R. Gilmore, The growth or collapse of a spherical bubble in a viscous compressible liquid. (1952).

[47] M.S. Plesset, A. Prosperetti, Bubble dynamics and cavitation. Annual Review of Fluid Mechanics, 9(1) (1977) 145-185.

[48] C.D. Ohl, M. Arora, R. Dijkink, V. Janve, D. Lohse, Surface cleaning from laser-induced cavitation bubbles. Applied physics letters 89(7) (2006b), 074102.

[49] V.J. Minsier, De. Wilde, J. Proost, Simulation of the effect of viscosity on jet penetration into a single cavitating bubble. Journal of Applied Physics, 106(8) (2009) 084906.

[50] Lamb, Hydrodynamics (6th Ed.), Cambridge University Press 1932.

[51] Q.X. Wang, The evolution of a gas bubble near an inclined wall. Theor. Comput. Fluid Dyn. 12(1) (1998) 29–51.

[52] Q.X. Wang, Numerical modelling of violent bubble motion. Phys. Fluids 16 (5) (2004) 1610-1619.

[53] A.Z. Zinchenko, M.A. Rother, R.H. Davis, A novel boundary-integral algorithm for viscous interaction of deformable drops. Physics of Fluids (1994-present), 9(6) (1997) 1493-1511.

[54] Y.L. Zhang, K.S. Yeo, B.C. Khoo, C. Wang, 3D jet impact and toroidal bubbles. J. Comput. Phys. 166 (2001) 336–360.

[55] Q.X. Wang, Unstructured MEL modelling of unsteady nonlinear ship waves. J. Comput. Phys. 210 (1) (2005) 183-224.

[56] C. Wang, B.C. Khoo, K.S. Yeo, Elastic mesh technique for 3D BIM simulation with an application to underwater explosion bubble dynamics. Computers & fluids, 32(9) (2003) 1195–1212.

[57] C. Wang, B.C. Khoo, An indirect boundary element method for three dimensional explosion bubbles. J. Comput. Phy. 194(2) (2004) 451–480.

[58] L. Rayleigh On the pressure developed in a liquid during the collapse of a spherical cavity. Philos Mag 34 (1917): 94–98.

[59] M.S. Plesset, A. Prosperetti, Bubble dynamics and cavitation. Annual review of fluid mechanics, 9(1) (1977), pp.145-185.

[60] M.S. Plesset, The dynamics of cavitation bubbles. Journal of applied mechanics 16 (1949): 277-282.

[61] W. Lauterborn, T. Kurz, Physics of bubble oscillations. Rep. Prog. Phys. 73 (2010)10650.

[62] H. Chen, W. Kreider, A.A. Brayman, M.R. Bailey, T.J. Matula, Blood vessel deformations on microsecond time scales by ultrasonic cavitation. Physical review letters, 106(3) (2011) 034301.

[63] H. Chen, J. Hwang, Ultrasound-targeted microbubble destruction for chemotherapeutic drug delivery to solid tumors J. Ther. Ultrasound. 1 (1) (2013)10.

[64] F. Sbeity, S. Ménigot, J. Charara, J.M. Girault,(2013) A General Framework for Modeling Sub-and Ultraharmonics of Ultrasound Contrast Agent Signals with MISO Volterra Series. Computational and mathematical methods in medicine.

[65] V. F. K. Bjerknes, Fields of Force (Columbia University Press, New York, 1906).

[66] A. A. Doinikov, Bjerknes forces and translational bubble dynamics. Bubble and Particle Dynamics in Acoustic Fields: Modern Trends and Applications (2005) ISBN: 81-7736-284-4.

[67] S. Zhang, J. H. Duncan, G. L. Chahine, The final stage of the collapse of a cavitation bubble near a rigid wall, J. Fluid Mec. 257 (1993) 147-181.

[68] S. Zhang, J. H. Duncan, On the nonspherical collapse and rebound of a cavitation bubble, Physics of Fluids (1994-present), 6(7) (1994) 2352-2362.

[69] J. P. Best, The formation of toroidal bubbles upon the collapse of transient cavities, J. Fluid Mec. 251 (1993) 79-107.

ACCEPTED MANUSCRIPT

[70] Q. X. Wang, K. S. Yeo, B. C. Khoo, K. Y. Lam, Strong interaction between buoyancy bubble and free surface, Theoret. and Comput. Fluid Dynamics 8 (1996b) 73.

[71] Q. X. Wang, K. S. Yeo, B. C. Khoo, K. Y. Lam, Vortex ring modelling for toroidal bubbles, Theoret. & Comput. Fluid Dyn. 19 (5) (2005) 303-317.

[72] A.M. Zhang, Y.L. Liu, Improved three-dimensional bubble dynamics model based on boundary element method. Journal of Computational Physics, 294 (2015) 208-223.

ACCEPTED MANUSCRIPT